crystals

MDPI

Article

Microstructure and Properties of Microwave-Sintered $Nd_2Fe_{14}B_p$/2024 Aluminum-Alloy–Co Composites

Tao Qin [1,2], Guirong Li [1,*], Hongming Wang [1], Wenxue Su [1], Chao Dong [1] and Jincheng Yu [2]

[1] School of Materials Science & Engineering, Jiangsu University, Zhenjiang 212013, China
[2] School of Mechanical Technology, Wuxi Institute of Technology, Wuxi 214121, China
* Correspondence: liguirong@ujs.edu.cn

Abstract: This study aimed at the preparation of a 2024 aluminum alloy (2024Al) matrix composite with high strength, high toughness and high magnetic properties that can be used in practical applications. Therefore, $Nd_2Fe_{14}B_p$/2024Al–Co composites with different Co contents (wt.%) were prepared by ball milling, cold isostatic pressing and microwave sintering. The effects of the Co content on the microstructure, mechanical properties and magnetic properties of the prepared composites were studied. Under the conditions of the sintering temperature of 490 °C, heating rate of 20 min/°C and soaking time of 30 min, it was found that with the increase in Co content (0→2.5%→5%→7.5%→10%), the grain size first decreased and then increased, and reached the optimal value of about 3–5 μm when the Co content was 7.5%, with the microstructure being relatively uniform. At the same time, the compactness of the composite arrived at a maximum of 95.4%. The main particle phases in the composite were $Nd_2Fe_{14}B$, Nd_2 (Fe, Co)$_{14}B$ and Co particles. In the nanoindentation test, the interface strength of the 7.5% Co sample was significantly higher than that of the Co-free sample. In addition, the microhardness, yield strength and compressive strength of the 7.5% Co sample were 152 HV, 210 MPa and 269 MPa, respectively, which increased by 67%, 78% and 75%, respectively, compared with the Co-free sample. With the increase in Co content, the remanence (*B*r), coercivity (H_{cj}) and maximum magnetic energy product ((*BH*) max) of the composites first increased and then decreased. When the Co content was 7.5%, the three performance indicators reached their optimum values, which were *B*r: 0.20 (T), H_{cj}: 4.6 (kOe) and $(BH)_{max}$: 28.36 (kJ/m^3). The expected goal of the lightweight magnetic materials was achieved, and the action mechanism of Co addition in the composites was also analyzed in detail.

Keywords: aluminum matrix composites; microwave sintering; mechanical properties; magnetic performance

check for updates

Citation: Qin, T.; Li, G.; Wang, H.; Su, W.; Dong, C.; Yu, J. Microstructure and Properties of Microwave-Sintered $Nd_2Fe_{14}B_p$/2024 Aluminum-Alloy–Co Composites. *Crystals* **2022**, *12*, 1493. https://doi.org/10.3390/cryst12101493

Academic Editor: Cyril Cayron

Received: 2 October 2022
Accepted: 18 October 2022
Published: 20 October 2022

Publisher's Note: MDPI stays neutral with regard to jurisdictional claims in published maps and institutional affiliations.

Copyright: © 2022 by the authors. Licensee MDPI, Basel, Switzerland. This article is an open access article distributed under the terms and conditions of the Creative Commons Attribution (CC BY) license (https://creativecommons.org/licenses/by/4.0/).

1. Introduction

With the rapid development of science and technology, magnetic materials continue to play an increasingly prominent role in modern military, automobile, production automation and daily life. At the same time, people continue to put forward higher requirements for lightweight magnetic materials with high efficiency and low energy consumption. For example, automobiles are developing towards being lightweight, miniaturization and electronization. However, existing magnetic materials, such as $Nd_2Fe_{14}B$, show very good magnetic properties but with high density. More importantly, their mechanical properties are not satisfactory, and they also have some disadvantages, such as poor processing technology, inferior corrosion resistance, low thermal conductivity and low electrical conductivity. Therefore, researchers are committed to developing magnetic materials with light weight, high strength, high toughness and high magnetism.

Aluminum is a non-ferrous metal with the largest output and is widely used in construction and structure, power electronics, durable consumer goods, packaging containers, machinery and equipment, transportation and other industries. It is a light metal with

low density and good ductility. Pure aluminum can be directly used as a material in many fields where a strength below 200 MPa is required. In order to improve the strength or comprehensive performance, one or more alloying elements can be added to aluminum, which is called aluminum alloy. Compared with pure aluminum, the structure and properties of aluminum alloys are different, and they are suitable for various processing materials or casting parts. However, neither pure aluminum nor aluminum alloy is magnetic, and they can only be used in non-magnetic applications, which greatly limits their application in the field of magnetic materials. Endowing aluminum and its alloys with magnetic properties will break tradition, realize the lightweight of magnetic materials and expand their applications in new industries and new fields. In this paper, a new type of aluminum matrix composite material was prepared with 2024Al as the matrix and hard $Nd_2Fe_{14}B$ particles as the magnetic composite phase, which had the characteristics of high magnetic properties, high toughness and light density. The research and development of the $Nd_2Fe_{14}B$/2024Al composite material will help 2024Al to enter the application range of magnetic devices, so as to give full play to its lightweight advantages. For example, if motor rotors widely used in new energy vehicles are made of magnetic aluminum alloy, their weight can be greatly reduced, the flexibility of acceleration and braking can be enhanced and the battery life can be increased dramatically.

For a long time, researchers have devoted themselves to improving the magnetic properties of magnetic materials [1,2]. However, domestic reports on magnetic aluminum alloys are still lacking, and foreign researchers have tried to study it, but the results are few. In 1978, the Research Office of the Faculty of Production Engineering, Nihon University, added magnetic powder ferrite to molten aluminum in order to prepare magnetic aluminum, however, the ferrite reacted with aluminum to form compounds at a high temperature, resulting in serious loss of magnetism. In 1987, the Kobe Steel Research Institute of Japan used magnetic powder solidification molding technology to produce magnetic aluminum, but the magnetic properties were far from the requirements, and the performance was unstable, which could not guarantee the mechanical properties such as strength and elastic modulus [3]. In 2013, Chandan [4] prepared a composite with magnetic $CoFe_2O_4$ nanoparticles dispersed in an aluminum matrix. When the content of $CoFe_2O_4$ reached 10%, the magnetization was 17.07 emu/g and the coercivity was 0.058 T, however, the magnetic properties of the reinforcement particles were insufficient, and the conventional sintering process led to a low density of the structure and poor uniformity of particle distribution. In 2015, A. Fathy et al. [5] studied the effects of powder metallurgy on the microstructure, mechanical properties and magnetic properties of aluminum matrix composites. After adding Fe, the structure of the composite was more uniform, and the sample had magnetic properties. The magnetization of the sample containing 10 wt.% Fe reached 0.6597 emu/g, but it still did not meet the requirements for use.

In previous work, researchers have tried to add fine $Nd_2Fe_{14}B$ particles to an aluminum melt, but due to the high temperature, the $Nd_2Fe_{14}B$ particles reacted with the aluminum matrix to form complex metal compounds, resulting in the reduction in the magnetic properties of $Nd_2Fe_{14}B$. Researchers have also studied the reaction between aluminum and NdFeB. Sadullahoglu, G. et al. studied the addition of Al and Cu in Nd–Fe–B magnets, indicating that the addition of Al was pressed at 750 °C to form a ternary FeNdAl composition [6], which brought some inspiration to our work. Compared with traditional sintering methods, microwave sintering (MWS) has the characteristics of low temperature, fast sintering, uniform temperature and selective sintering. In the 1980s, microwave sintering technology gradually received attention and was introduced into the field of materials science and began to be used to prepare various high-performance ceramics by sintering [7]. At present, microwave sintering technology has been widely used in the preparation of metal matrix composites. Hongming Wang et al. prepared an $FeCoNi_{1.5}CrCu$/2024Al composite by microwave sintering. When the sintering time was 40 min, the mechanical properties of the material reached the optimum [8]. M.G.Ananda Kumar prepared aluminum cenosphere powder metallurgy composites by microwave

sintering. The results showed that microwave sintering could obtain better mechanical properties than traditional sintering [9].

Our research group has previously tried to prepare $Nd_2Fe_{14}B$ /Al composites by powder metallurgy and microwave sintering. The microwave sintering process was studied, and the addition amount of Nd2Fe14B was optimized [10,11]. The prepared composites achieved the expected goals in terms of mechanical properties and magnetic properties, laying a good foundation for further research. However, the chemical properties of pure aluminum are too active, it is easily oxidized and it has poor mechanical properties. Although it has good ductility, it is not suitable for structural materials. The compound 2024Al is a typical Al–Cu–Mg series hard aluminum alloy with the characteristics of high strength, good heat resistance, excellent damage resistance and good formability. Nevertheless, with the development of technology and industry, pure 2024Al has been unable to meet the performance requirements of various industries for some important applications. In order to further improve the mechanical properties of the material, researchers from various countries have tried to add reinforcing phase particles to the matrix alloy material to form particle-reinforced aluminum matrix composites [12,13]. However, the research on realizing the magnetic properties of 2024 aluminum alloy is still lacking at home and abroad.

In this article, novel $Nd_2Fe_{14}B$/2024Al–Co composites with different Co contents were fabricated by powder metallurgy. Mixed powders were made into samples by high-energy ball milling, cold isostatic pressing and microwave sintering. The manufacturing process, microstructure, interface strength, mechanical properties and magnetic properties of the composites were studied in detail by using modern testing technology. In addition, the mechanism of action of Co in the composites was discussed. The purpose of this work was to prepare magnetic aluminum matrix composites that can be used in practical applications, and to provide a reference for the future preparation of aluminum matrix composites with excellent mechanical and magnetic properties.

2. Experimental Procedure

The raw materials for the experiment were commercial powders of 2024Al, $Nd_2Fe_{14}B$ and Co with a purity of 99.9%, of which the particle size of the 2024Al powder was below 5 μm, and the particle size of the Co and $Nd_2Fe_{14}B$ was below 45 μm. Table 1 presents the experimental scheme for preparing the new $Nd_2Fe_{14}B$/2024Al–Co composites. Figure 1 shows the morphology of the three powders and the shape and size of the obtained sample.

Table 1. Experimental scheme for the preparation of $Nd_2Fe_{14}B$/2024Al–Co composites (wt.%).

Serial No.	2024 Aluminum Alloy	$Nd_2Fe_{14}B$	Co
0	80.0	20	0
1	77.5	20	2.5
2	75.0	20	5.0
3	72.5	20	7.5
4	70.0	20	10.0

First, the powder was mixed according to the ingredient ratio, and then put in the high-energy ball mill for ball milling. The optimized ball-milling process obtained through the previous experiments was as shown in Table 2.

After ball milling, the mixed powder was put into a vacuum-drying oven evenly for dehydration at 65 °C. Then, the dehydrated powder was filled into a rubber mold, and then put into the cold isostatic pressing equipment. When cold isostatic pressing was performed, two independent powerful magnets were placed at the top and bottom of the mold for magnetic isostatic pressing. This was to enable the preliminary magnetic orientation of the $Nd_2Fe_{14}B$ particles in the mixed powder during the pressing process. The mixed powder in the mold withstood a pressure of 300 MPa for 2 min. Figure 1b demonstrates the obtained sample and its dimensions.

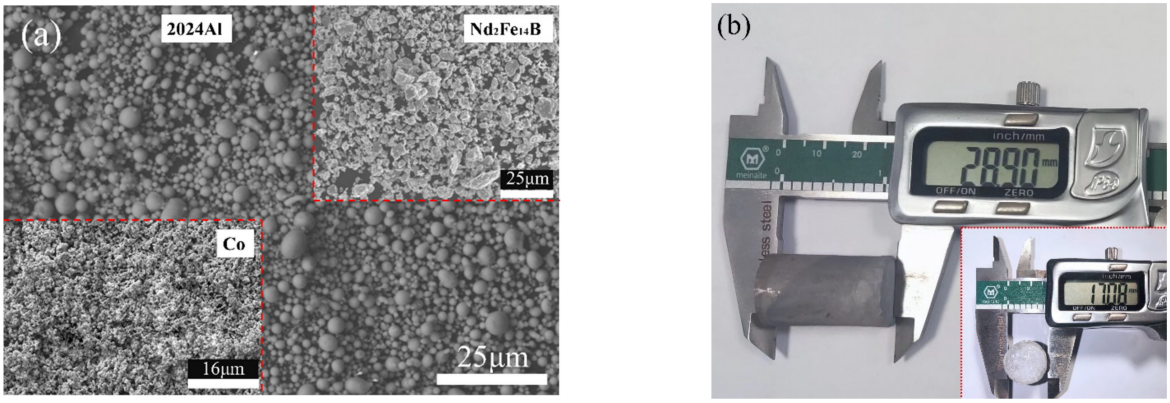

Figure 1. Morphology of 2024Al, $Nd_2Fe_{14}B$ and Co powders (**a**) and the shape and size of the obtained sample (**b**).

Table 2. The technological parameters of ball-milling process.

Parameters	Level
Balls-to-materials ratio	5:1
Large balls to medium balls to small balls ratio	1:2:4
Alcohol-to-powder material ratio	2:3
Milling time	5 h

The pressed samples were sintered in a microwave sintering furnace protected by an argon atmosphere. The output power of the microwave sintering equipment was 4 kW, and the frequency was 2.45 GHz. The heating temperature, heating speed and holding time were 490 °C, 20 °C/min and 30 min, respectively. Figure 2 shows the microwave sintering schematic diagram and a comparison of the microwave sintering curve with ordinary sintering and spark plasma sintering (SPS). It shows that microwave sintering has more advantages in terms of rapid heating. In an adiabatic environment, without considering the reaction heat and phase transition heat during the heating process, the heating rate dT/dt per unit volume of material in the presence of a microwave field can be expressed as Equation (1) [14]:

$$\frac{dT}{dt} = \frac{2\pi f \cdot \varepsilon_0 \cdot \varepsilon \cdot E^2}{C_p \cdot \rho} \quad (1)$$

where dT/dt is the heating rate (K/s), T is the thermodynamic temperature (K) and t is the heating time. f is the microwave frequency, here 2.45 GHz; ε_0 represents the vacuum dielectric constant, and the value is 8.85×10^{-2} F/m; ε is the dielectric loss factor of materials; E is the electric field intensity of the microwave(V/m); C_p is the heat capacity of the target materials (J/K) and ρ is the density of target material (kg/m^3). It can be seen from Equation (1) that the heating rate of microwave sintering is related to electric field intensity E, heat capacity C_p and density ρ.

After sintering, the specimens were mechanically polished and then corroded by Keller reagent (1%HF + 1.5%HCl + 2.5%HNO_3 + 95%H_2O). The microscopic morphology of the samples was observed by an S-3400 N scanning electron microscope (SEM). Phase analysis of the sample surface was conducted by a D8 ADVANCE X-ray diffractometer (XRD), and the diffraction angle range was 10°–90° with a scan speed of 5°/min.

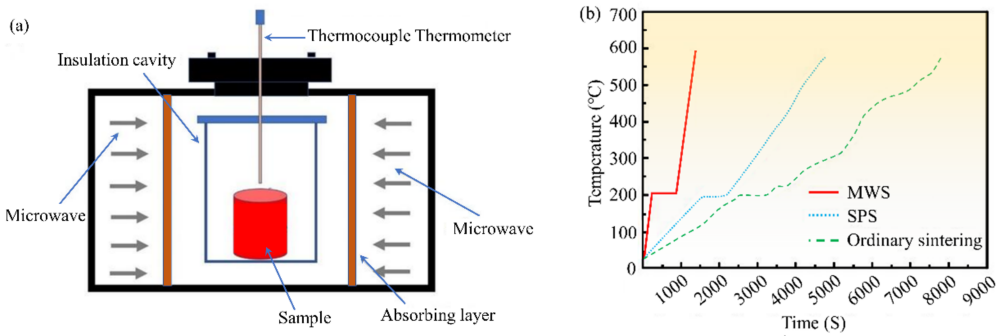

(**a**) (**b**)

Figure 2. Schematic diagram of microwave sintering (**a**) and comparison of the heating velocity among three sintering methods (**b**).

The compactness of the 1 cm × 1 cm × 1 cm composite block was obtained experimentally based on Archimedes' principle. First, the prepared bulk composite material was dried in a vacuum-drying oven at low temperature to a moisture-free state, and then the mass in the air was accurately measured many times by an analytical balance with 0.1 mg accuracy and the average value was obtained as G_1. Next, the composite block was tethered with a thin wire and immersed in pure distilled water without impurities, and the mass in the distilled water was measured as G_2. The actual density of the sample can be calculated by Equation (2):

$$\rho = \frac{G_1}{G_1 - G_2} \cdot \rho_{water} \tag{2}$$

where ρ_{water} denotes the density of the water under the conditions of the tested water temperature. The theoretical density ρ_0 of the composite can be calculated by Equation (3)

$$\rho_0 = \sum \rho_i . v_i \tag{3}$$

where ρ_i stands for the theoretical density of i phase, and v_i denotes the volume fraction. Then, the compactness I can be obtained from Equation (4):

$$I = \frac{\rho}{\rho_0} \tag{4}$$

The hardness of the samples was obtained by a DYDHV-1000 Vickers hardness tester, and the load was 9.8 N during measurement. Each sample was measured at least 5 times, and then the average value was calculated as the effective value. In addition, the mechanical property test was carried out on a DDL100 electronic universal testing machine.

Before the magnetic properties test, the samples were magnetized by TSK-H2060 voltage-regulating magnetization equipment, and the magnetic induction intensity B was set to 3 T. The magnetic properties were tested using the magnetic property testing system manufactured by Quantum Design, Inc. in the United States. The indentation hardness and elastic modulus of the samples were tested by a nanoindentation hardness tester (TTX-NHT3).

3. Results and Discussion

3.1. Microstructure

Figure 3 presents the SEM images of the $Nd_2Fe_{14}B$/2024 aluminum-alloy–Co composites with different Co contents: 0% (Figure 3a), 2.5% (Figure 3b), 5% (Figure 3c), 7.5% (Figure 3d) and 10% (Figure 3e). The Co-containing composites exhibited some characteristics in comparison to the Co-free sample.

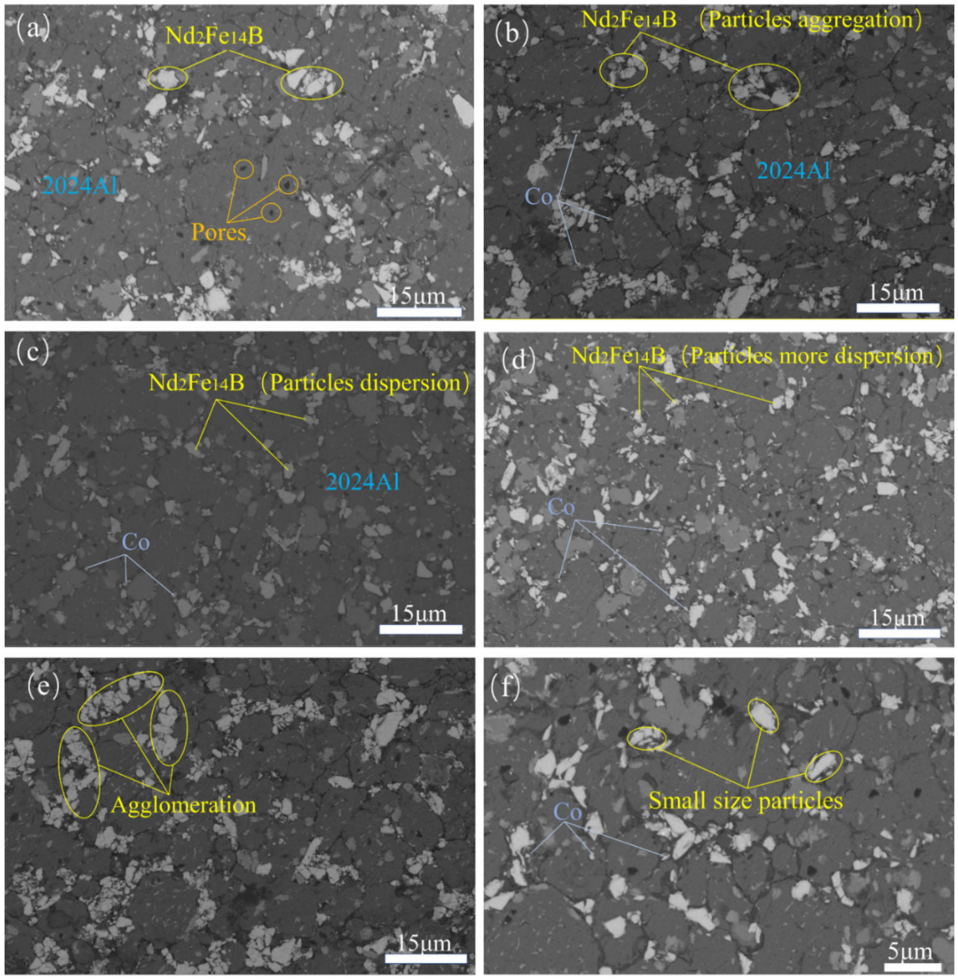

Figure 3. Effects of the Co content on the microstructure of composites: (**a**) 0%, 2500×; (**b**) 2.5%, 2500×; (**c**) 5%, 2500×; (**d**) 7.5%, 2500×; (**e**) 10%, 2500×; (**f**) 7.5%, 5000×.

Firstly, the grain size of the samples changed. The average grain size of the Co-free sample was about 15 μm. The grain size of the 2.5% sample was equivalent to that of the Co-free sample, but the $Nd_2Fe_{14}B$ particles were more evenly distributed. With the increase in the Co content, the gain size of the 5% and 7.5% samples decreased gradually, especially for the 7.5% sample, where most of the grains were around 3–5 μm in size (Figure 3f), which revealed that Co played a role in refining the matrix grains. It was analyzed that the added Co particles, as the core of the heterogeneous nucleation, promoted nucleation and inhibited the growth of matrix grains, resulting in grain refinement.

For the second microstructural characteristic, the $Nd_2Fe_{14}B$ particles became finer and more evenly distributed. When the Co content reached 10% (Figure 3e), the $Nd_2Fe_{14}B$ particles appeared to be agglomerated and were connected to each other and grew locally. This was not conducive to the combination of the $Nd_2Fe_{14}B$ particles and the 2024Al matrix and the formation of a good interface.

Furthermore, the phase change of the materials was discussed by EDS. Figure 4 presents the microstructure and energy diffraction spectrum (EDS) in the typical regions of the 7.5% Co composite. The EDS energy spectrum analysis was performed on the spots A and B marked in Figure 4a, respectively, and the results are shown in Figure 4g,h, indicating that the composition of spot A and spot B were $Nd_2Fe_{14}B$ particles and the 2024 aluminum alloy matrix, respectively. It can be seen from Figure 4f that the diffusion of Co element into the $Nd_2Fe_{14}B$ particles was relatively obvious. However, Al element in the matrix did not diffuse into the $Nd_2Fe_{14}B$ particles (Figure 4b). When the content of Co was low, it was only distributed in the matrix. With the increase in the content of Co, some Co atoms

entered the $Nd_2Fe_{14}B$ phase, replacing Fe atoms and forming the $Nd_2(Fe,Co)_{14}B$ phase; the other Co atoms entered the grain boundary and combined with Nd to form a Co-rich phase [15], which enhanced the chemical stability of the interface between the $Nd_2Fe_{14}B$ particles and the 2024Al matrix. Moreover, the formation of this strong magnetic phase is an important factor for the enhancement of the magnetic properties of the composite.

In addition, Co atoms were dispersed and distributed on the 2024Al matrix, which played a role in terms of solid solution strengthening. In addition, some Co atoms were attached to the surface of the $Nd_2Fe_{14}B$ particles as the active element, which improved the wettability between the $Nd_2Fe_{14}B$ particles and the 2024Al matrix. As shown in Figure 4d, the content of Nd element in the marked area was obviously larger, which corresponded to the $Nd_2Fe_{14}B$ particles, while there was a certain amount of Nd in other areas, and the distribution was relatively uniform, which indicated that the Nd-containing phases were in the matrix, and the distribution was more even. Figure 4c,e shows the distribution of B and Fe elements, respectively, where they were basically consistent with the distribution of Nd element, which indicated the integrity of the $Nd_2Fe_{14}B$ particles in the composite.

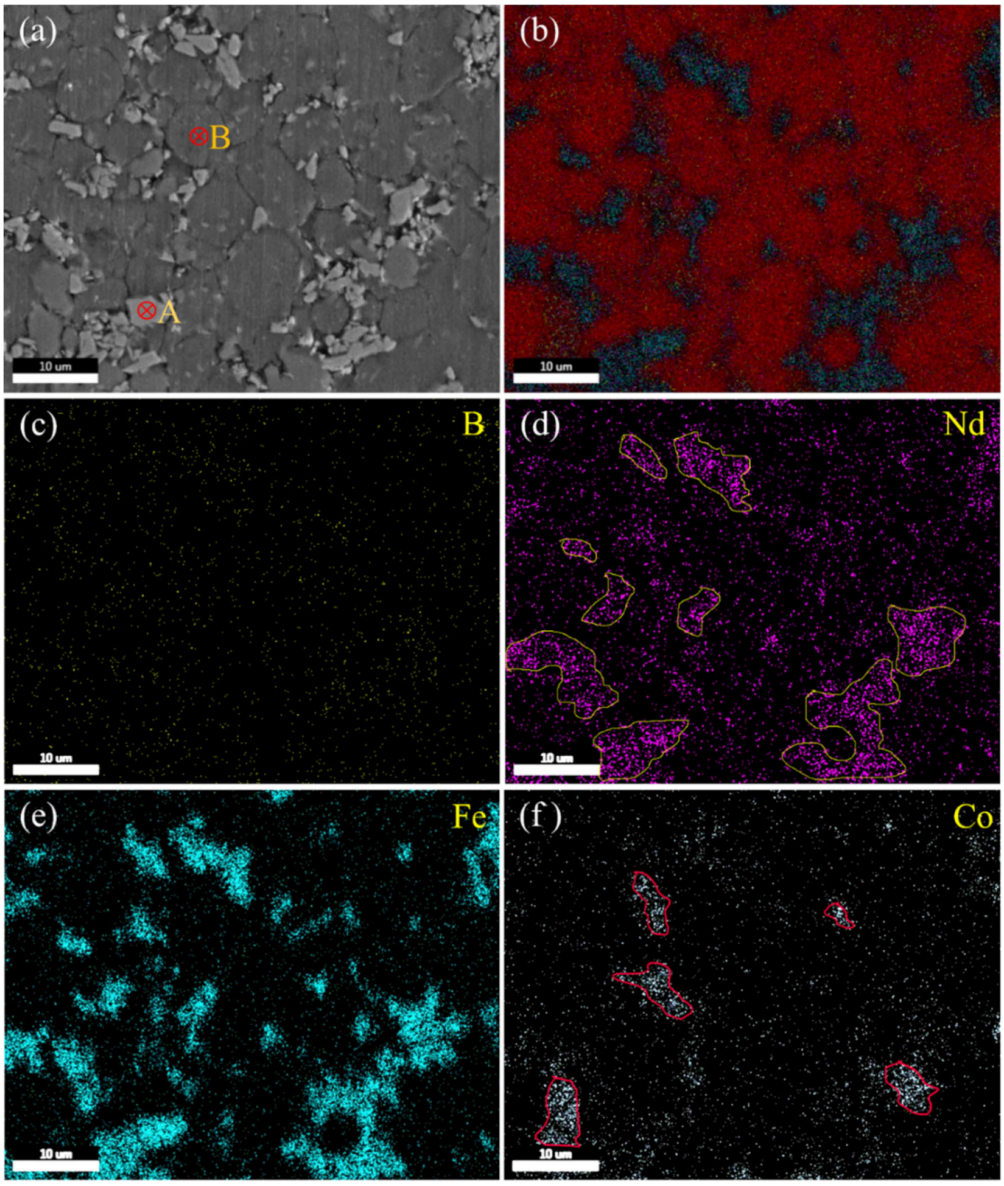

Figure 4. *Cont.*

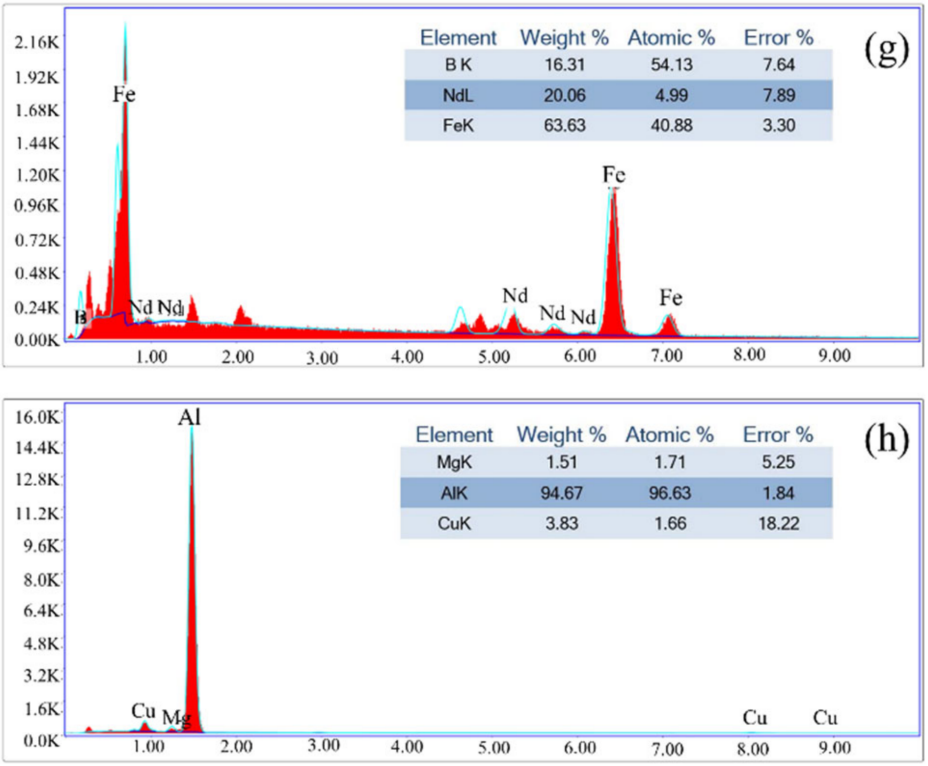

Figure 4. Surface-scanning images of the $Nd_2Fe_{14}B$/2024Al–Co composite. (**a**) overall view map; (**b**) overall scanning; (**c**) B; (**d**) Nd; (**e**) Fe; (**f**) Co (**g**) Element composition at spot A; (**h**) Element composition at spot B.

3.2. XRD Analysis

Figure 5 shows the XRD patterns of the $Nd_2Fe_{14}B$/2024Al composites with different Co contents. When the Co content was 2.5%, other new phases such as metal compounds did not appear in the composite. Since the sintering temperature was 490 °C, which is lower than the melting point of aluminum, and the melting point of $Nd_2Fe_{14}B$ is 1350 °C, the thermodynamic conditions for chemical conditions were insufficient. The sintering process was carried out in a vacuum protective atmosphere, which effectively inhibited the oxidation behavior of the 2024Al matrix, and it was not easy to generate oxides. When the Co content increased to 5% and 7.5%, the Co–Fe phase appeared in the XRD pattern (Figure 5a), which was due to the reaction of Co with Fe in the $Nd_2Fe_{14}B$. The mixture of the soft magnetic Co–Fe phase and the hard magnetic $Nd_2Fe_{14}B$ phase is an ideal material for exchange coupling magnets, and both single phase and composite magnets exhibit a significant remanence enhancement [16]. In the XRD pattern (Figure 5b), the $Nd_2Fe_{14}B$ in the composites with different Co contents did not change or shift, indicating that the structure of the $Nd_2Fe_{14}B$ was relatively stable during the sintering process. This was conducive to the exertion of the magnetic properties of the $Nd_2Fe_{14}B$ particles [17].

However, single phase Co was not detected in the composite material. Firstly, the content of Co was low, and the distribution was relatively dispersed, resulting in low X-ray diffraction peaks that were difficult to observe. Secondly, the positions of the triplet peaks of Co and Al were relatively close. In the 2024Al matrix, the triplet peaks of Co may have been covered by those of Al.

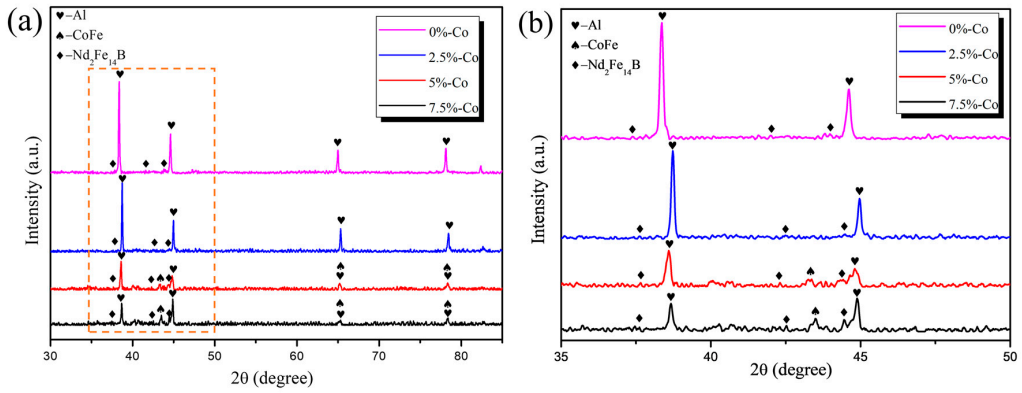

Figure 5. XRD pattern of $Nd_2Fe_{14}Bp$/2024Al–Co composites: (**a**) XRD pattern; (**b**) magnified XRD of the short wireframe area.

3.3. Interface

The micro–nano mechanical properties of the interface micro-zone are an important index of the interface bonding state. In order to study the effect of Co on the interface strength of the composites, the interface area between the composite matrix and the reinforcement was characterized by a quasi-static nanoindentation test. Figure 6 is the result of the interfacial nanoindentation test. The load–displacement (P–h) curve can be analyzed using Oliver and Phar's theorem [18] to obtain the nanohardness (H) and elastic modulus (E). The H can be calculated using Equations (5)–(9) [19].

$$H = \frac{P_{max}}{A_c} \tag{5}$$

$$A_c = 25.4{h_c}^2 \tag{6}$$

$$h_c = h_{max} - \varepsilon\frac{P_{max}}{S} \tag{7}$$

$$h_s = \varepsilon P_{max}/S \tag{8}$$

$$S = \mathrm{d}P/\mathrm{d}h \tag{9}$$

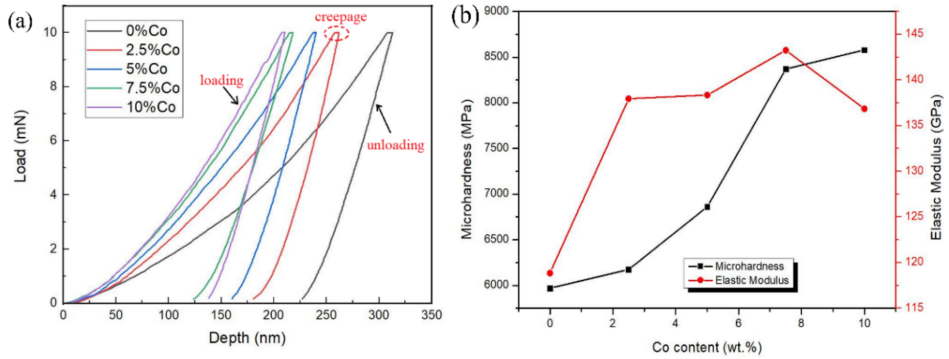

Figure 6. Load–displacement (P–h) curve (**a**) and the nanohardness and elastic modulus of the interface (**b**).

In the above formulas, P_{max} represents the maximum load (mN); A_c represents the contact area between the indenter and the sample (mm^2); h_c is the depth of full contact between the indenter and the sample; h_{max} is the maximum pressure depth (nm); h_s is the superficial displacement depth of the surrounding material around the contacting position for the indenter and sample; ε is the indenter parameter (For the Berkovich indenter, $\varepsilon = 0.72$) and S is the slope of the P–h curve.

Figure 6a shows the nanoindentation load–displacement (P–h) curves at the interfaces of the 0%Co, 2.5%Co, 5%Co, 7.5%Co and 10%Co composite specimens, respectively. As illustrated, under the same load conditions, with the increase in the Co content, the indentation depth of the indenter gradually decreased, and the indentation depths of the composite samples containing 7.5% and 10% Co were the shallowest, which meant the highest nanohardness. This shows that Co was helpful in promoting the wettability of the magnetic particles and the 2024Al matrix and could improve the interfacial bonding strength between the magnetic particles and the 2024Al matrix. The analysis suggests that, due to the addition of Co, the $Nd_2Fe_{14}B$ particles became fine and uniform, and the reinforcement particles had a greater impediment to dislocation slip. At the same indentation depth, the indentation hardness increased with decreasing particle size [20]. However, the elastic recovery distance of the 7.5% Co specimen was larger than that of the 10% Co specimen, indicating that the elastic deformation of the 7.5% Co sample at the interface was larger. In addition, from the point of view of the pressure-maintaining process, five groups of samples had different degrees of creep platforms, especially the 0% Co sample. It can be analyzed from the following two aspects: firstly, the creep of metal materials is mainly conducted by dislocation slip and grain boundary slip, and the creep at room temperature is mainly caused by intragranular dislocation slip. However, the grain boundary is an obstacle to dislocation slip. The larger the number of grain boundaries, the greater the resistance to dislocation movement, and the material is less prone to creep [21]; secondly, some Co atoms were dissolved in the 2024Al matrix to form a lattice distortion stress field around the Co atoms. This stress field interacted with the dislocation stress field, which hindered the dislocation movement, increased the creep resistance and improved the creep resistance of the composite.

Figure 6b is a graph showing the change trend of the nanohardness and elastic modulus at the interface of the composite. With the increase in the Co content, the nanohardness of the interface also increased gradually. The nanohardness of the 7.5% Co sample reached 8369.7 MPa, which was slightly lower than that of 10% Co sample. However, with the increase in the Co content, the interfacial elastic modulus of the composites first increased, reaching a peak value of 143.25 GPa at 7.5% Co, and then decreases, but was still much higher than that of the Co-free sample. Therefore, while the interface nanohardness was improved, the elasticity was lost to a certain extent. It is believed that the excessive Co content caused the agglomeration of the $Nd_2Fe_{14}B$ particles and induced cracks, which reduced the plastic deformation ability of the interface area, resulting in the decline in the elastic modulus, and finally affected the comprehensive mechanical properties of the interface micro area. Therefore, when the Co content was 7.5%, a high-quality interface structure was obtained, taking into account the simultaneous improvement of the strength and toughness, and the advantages of the mechanical properties of the composite were reflected.

3.4. Compactness

Figure 7 shows the effect of the Co content (0%, 2.5%, 5.0%, 7.5% and 10%) on the compactness of composites. It can be seen that the Co content had a significant effect on the compactness of the composites. When Co was not added, the compactness of the composite was 89.8%. With the increase in Co addition (2.5%→5%→7.5%→10%), the compactness increased first and then decreased. When the Co content was 7.5%, the highest compactness was 95.4%. In the process of cold isostatic pressing, due to the strong pressure, the approximately spherical Co particles could easily slide into the gap between the $Nd_2Fe_{14}B$ particles and the 2024Al matrix to fill the gap, as shown in Figure 8. When the Co content was 10%, the compactness of the composites decreased. The reason was that more Co adhered to the surface of $Nd_2Fe_{14}B$ particles, causing them to agglomerate and form larger particles, which increased the number of pores and eventually led to a decrease in the material's compactness.

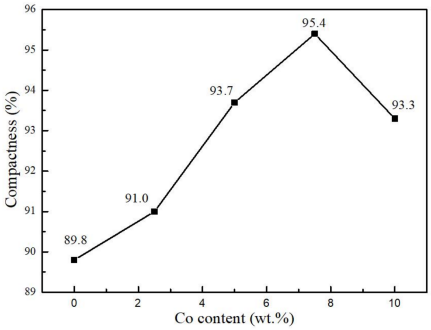

Figure 7. Influence of Co content on the compactness of the composites.

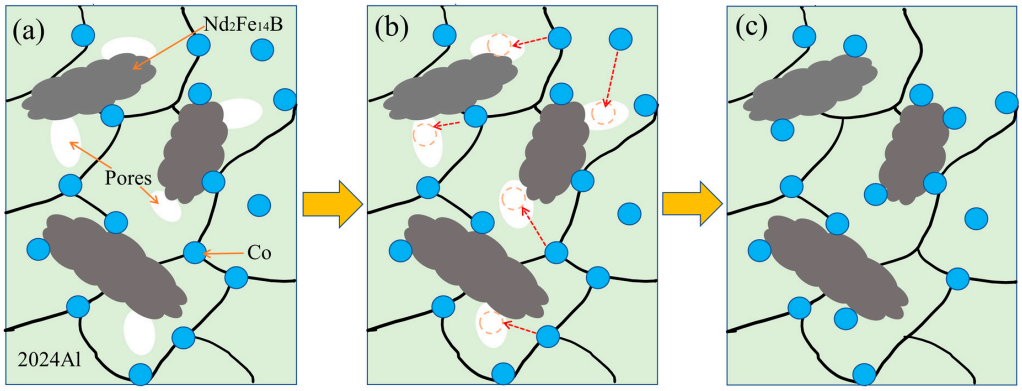

Figure 8. Schematic diagram of the densification process of the Co-containing composite powder. (**a**) The mixed powder was pressed under a low pressure; (**b**) the movement trend of Co atoms; (**c**) final position of Co atoms.

On the other hand, from the perspective of the thermal effect of microwaves, the absorption and coupling effects of different materials related to microwaves are related to their electrical conductivity and magnetic permeability [22]. The electromagnetic properties and penetration depth of each component in the composite are shown in Table 3. It can be seen that Co has both a high electrical conductivity and magnetic permeability. Therefore, during the microwave sintering process, Co more easily absorbed the microwaves and became a local hot spot. When the Co content exceeded 7.5%, hot spots appeared around a large amount of Co particles, and the pores expanded and were difficult to discharge from the composite.

Table 3. Electromagnetic properties and penetration depth (δ) of each component in the composite.

Phases	Conductivity σ (S/m)	Magnetic Permeability μ (H/m)	δ at Room Temperature(μm)	δ at 853 K (μm)
$Nd_2Fe_{14}B$	5.30×10^5	1.28×10^{-6}	13.40	72.70
Al	3.53×10^7	1.26×10^{-6}	1.70	9.20
Co	1.50×10^7	2.19×10^{-4}	0.20	1.07

In addition, the penetration depth δ of the microwaves in the sample can be calculated by Equation (10) [23]:

$$\delta = \frac{1}{\sqrt{\pi f \sigma \mu}} \quad (10)$$

where f denotes the microwave frequency (2.45 GHz), σ is the conductivity of the material(S/m) and μ is the magnetic conductivity (H/m). Therefore, with the increase in σ and μ, the penetration depth of microwave δ decreases.

For metallic materials, the surface penetration depth is related to temperature, which can be expressed by Equation (11):

$$\delta' = \sqrt{\frac{2K}{f\sigma\mu}} \tag{11}$$

where δ' denotes the penetration depth at a higher temperature T, and K denotes the temperature coefficient, which can be calculated using Equation (12) [24]:

$$K = 1 + \frac{T - 20}{234.5} \tag{12}$$

where T is the thermodynamic temperature. Therefore, when the temperature T increases, K increases, and the penetration depth δ' also increases. Table 3 also gives the penetration depth values of each phase at room temperature and 853 K. As can be seen, the penetration depth of $Nd_2Fe_{14}B$ particles was the highest among the three, especially at 853 K, which meant that the $Nd_2Fe_{14}B$ and the Co attaching to its surface could completely absorb the microwave energy and accumulate more heat in local areas. The local high temperature also caused an expansion of the pores, which was not conducive to the discharge of the gas. These two aspects were also the reasons for the decrease in the compactness.

3.5. Hardness and Compressive Strength

Figure 9 shows the microhardness, yield strength and compressive strength of the composites obtained with different Co contents. As shown here, with the increase in Co content, the three parameter values increased and then decreased. When the Co content was 7.5%, the microhardness, yield strength and compressive strength reached the maximum, which were 152.0 HV, 210.0 MPa and 269.0 MPa, respectively.

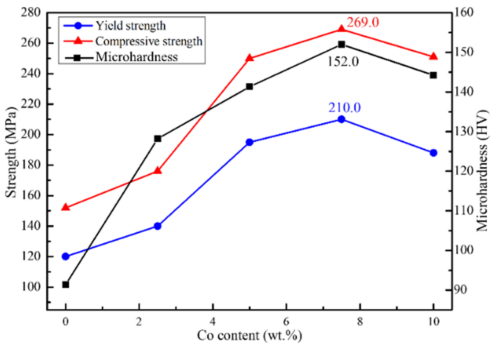

Figure 9. Microhardness, compression and yield stress of the composites with different Co contents.

As mentioned above, the addition of Co improved the compactness of the composites, especially when the Co content reached 7.5%, where the compactness was the highest, and the hardness and compactness are closely related. In addition, the Co particles attaching to the grain boundaries could hinder the movement of dislocations and played a pinning role. Other Co particles dispersed in the 2024Al matrix could produce a dispersion-strengthening effect. However, when the content of Co was higher than 7.5%, the formation of an agglomerated Co phase significantly reduced the effect of dispersion strengthening.

Compared with the Co-free sample, the amplifications of the yield strength and compressive strength were 78% and 75%, respectively. When the Co content arrived at 10%, the yield strength and compressive strength decreased to some extent. The strengthening mechanism of Co addition can be analyzed from the following aspects.

First, it can be seen from Section 3.1 that the addition of Co refined the grains of the composites. The grain size of the 7.5% Co sample was only 3–5 μm, which was close to the particle size of the 2024Al particles after ball milling. In other words, the microwaving sintering did not prompt the growing of the matrix size due to its rapid heating characteris-

tics. Based on the classical Hall–Petch (H–P) equation, the relationship between the yield strength σ_y and the average grain diameter d can be expressed by Equation (13) [25]:

$$\sigma_y = \sigma_0 + kd^{-1/2} \quad (13)$$

where σ_y denotes the yield strength corresponding to the 0.2% strain; σ_0 denotes the lattice frictional resistance when moving a single dislocation; k denotes a constant value, 68 MPa·μm$^{1/2}$ for aluminum alloys and d denotes the average grain diameter. According to Equation (13), the yield strength σ_y is inversely proportional to the square root of the grain diameter d. The H–P formula is mainly based on the grain boundary hindering dislocation slip. After grain refinement, due to the increase in the ratio of the grain boundary, the effect of the grain boundary hindering dislocation slip is strengthened, and the stacking of dislocations near the grain boundary leads to the increase in the yield strength and tensile strength of the alloy with grain refinement. As shown in Figure 10, more dislocations can be accumulated inside large grains to generate the driving force to move dislocations from one grain to another. Therefore, it is easier for dislocations to move in large grains than in small grains, and small-grained materials exhibit a higher yield strength [26].

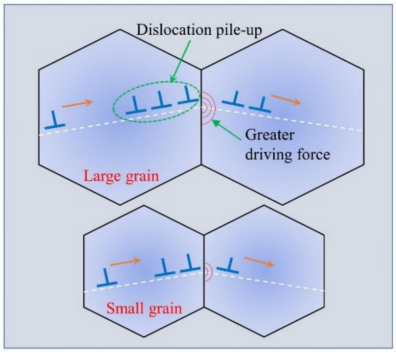

Figure 10. Schematic diagram of the movement of dislocations within the grain.

Second, as a surface-active element, the Co improved the interface bonding strength between the $Nd_2Fe_{14}B$ particles and 2024Al matrix, which was helpful in exerting the interface-strengthening mechanism. When the amount of Co added continued to increase, the compressibility of the material decreased because too many Co particles gathered to form larger Co particles. The existence of these large particles weakened the two strengthening mechanisms mentioned above and seriously affected its mechanical properties.

3.6. Magnetic Properties

Figure 11 shows the VSM curve of the $Nd_2Fe_{14}B$/2024Al–Co composites with different Co addition amounts. The magnetic properties of the material, such as the remanence (Br), coercivity (H_{cj}) and magnetic energy product ((BH) max) can be calculated from the VSM curve. Figure 12 presents the variation trend of the magnetic properties of the composites with different Co contents. As can be seen, the addition of Co changed the magnetic properties of the composites. With the increase in the Co content, the remanence (Br), coercivity (H_{cj}) and magnetic energy product ((BH) max) of the composites first increased and then decreased. When the Co content was 7.5%, the three performances were optimal, which were Br: 0.20 T, H_{cj}: 4.6 kOe and (BH) max: 28.36 (kJ/m^3). When the Co content was 10%, the performances decreased. The influence of the Co on the change in the magnetic properties of the composite material is mainly as follows:

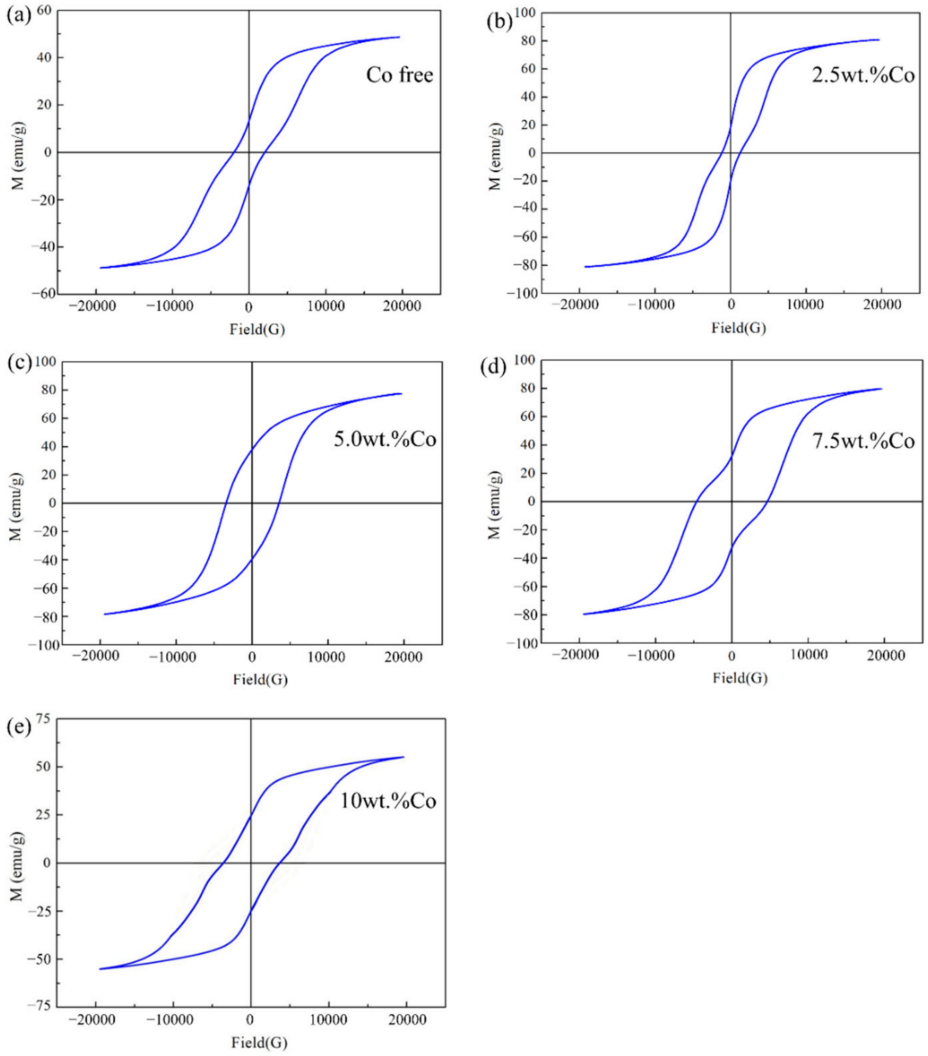

Figure 11. VSM curve of the composites with different Co contents. (**a**) Co free; (**b**) 2.5wt.%Co; (**c**) 5.0wt.%Co; (**d**) 7.5wt.%Co; (**e**) 10wt.%Co.

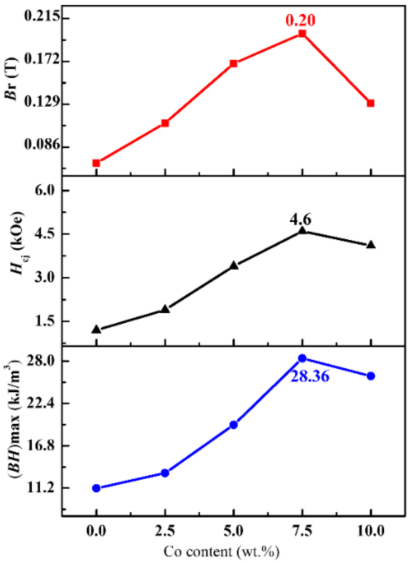

Figure 12. Effect of the Co content on the magnetic properties of the composites.

First, an important factor that affects the magnetic properties of composites is the compactness, which reflects the bonding strength of the 2024Al matrix and the $Nd_2Fe_{14}B$ particles. The relevant literature shows that the bonding ability between magnetic particles and the matrix will affect the magnetic properties of composites [27]. In the process of magnetizing the composite, uneven and dispersed magnetic fields will be formed in the pores inside the material. These scattered magnetic fields will produce a reverse magnetization effect, as shown in Figure 13. Therefore, when the compactness is increased, the number of blowholes in the composite is reduced, which means that the corresponding reverse magnetization region is reduced, and the remanence (*Br*) and magnetic energy product ((*BH*) max) of the material will be improved. When the compactness decreases due to the continuous increase in Co content, the corresponding performance parameter also decreases.

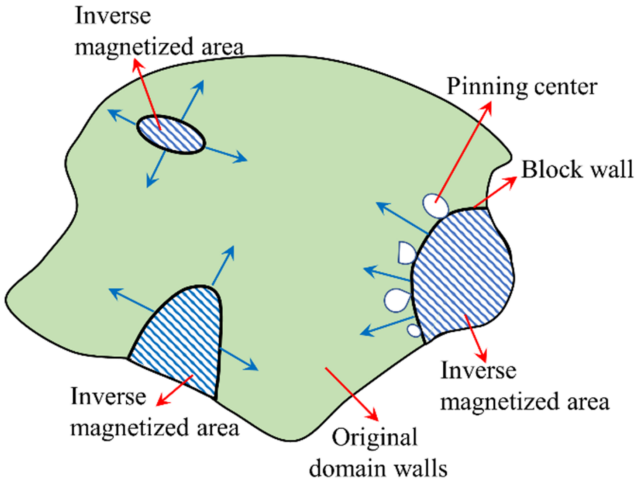

Figure 13. Schematic diagram of magnetization and inverse magnetization.

Second, the Co phase is a soft magnetic phase, while the $Nd_2Fe_{14}B$ phase is a hard magnetic phase, and there will be interactive coupling between them. Specifically, Co particles with soft magnetism were dispersed around the $Nd_2Fe_{14}B$ phase. When there is an external magnetic field, the magnetic moment of the atoms of the soft magnetic phase will turn to the direction consistent with the magnetization direction of the $Nd_2Fe_{14}B$ phase (Figure 14a). However, when the magnetic field is removed (Figure 14b), the magnetic moment of the Co particles around the $Nd_2Fe_{14}B$ phases will rotate under the influence of the magnetic moment of $Nd_2Fe_{14}B$ and be pinned in the average direction of the $Nd_2Fe_{14}B$ magnetic moment, which helps to improve the remanence of the composite (Figure 14c). For those Co particles far away from the $Nd_2Fe_{14}B$ particles, after removing the external magnetic field, their atomic magnetic moments are not easily pinned and deflected. The deflected magnetic moment may be inconsistent with the average magnetic moment direction of the $Nd_2Fe_{14}B$ particles (Figure 14d), which will affect the magnetic properties of $Nd_2Fe_{14}B$ phases. Therefore, when the content of Co was lower than 7.5 wt.%, the number of soft magnetic phases was small, and the magnetic moment of different directions had little effect on the magnetic moment of the $Nd_2Fe_{14}B$ particles. Based on the interaction between soft and hard magnetic particles, the magnetic properties of the composites were improved. When the content of Co exceeded 7.5 wt.%, a large amount of soft magnetic phases far away from the $Nd_2Fe_{14}B$ phases will obviously weaken the magnetic moment of the hard magnetic phases, which may lead to the decrease in the magnetic properties of the composite.

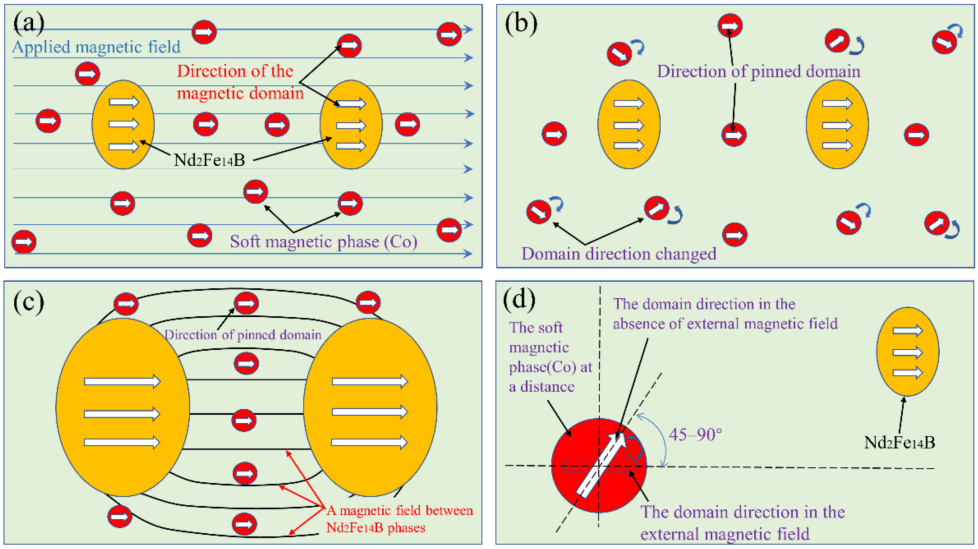

Figure 14. Schematic diagram of magnetic interaction coupling between $Nd_2Fe_{14}B$ phases and Co particles. (**a**) External magnetic field is applied; (**b**) The magnetic moment of the Co particles rotates; (**c**) The Co particles around the Nd2Fe14B phases are pinned; (**d**) The magnetic moment of the Co particles far away from the Nd2Fe14B particles.

Table 4 compares the magnetic properties of $Nd_2Fe_{14}B$, ferrite and the optimized sample in this experiment. The results showed that the optimized sample of $Nd_2Fe_{14}B$/2024Al-Co composite prepared by microwave sintering had certain magnetic properties. Although it was lower than the $Nd_2Fe_{14}B$ permanent magnet, its coercivity (H_{cj}) and magnetic energy product ((*BH*) max) were slightly higher than those of the ferrite. The purpose of the "magnetic aluminum matrix composite" in the material design was initially realized. Moreover, the density of the optimized sample was only 4.15 g/cm^3, which was far lower than the density of the $Nd_2Fe_{14}B$ permanent magnet and ferrite, and the goal of "lightweight magnetic materials" was also preliminarily realized. In the next research, the authors will try to further improve the magnetic properties and mechanical properties of the alloy by alloying and rolling

Table 4. Magnetic properties of $Nd_2Fe_{14}B$, ferrite permanent magnets and the optimal sample.

Magnetic Material	Density (g/m^3)	*Br* (T)	H_{cj} (kOe)	(*BH*) Max (kJ/m^3)
$Nd_2Fe_{14}B$	7.55	1.26	12.1	270
Ferrite	7.80	0.31	3.3	25
Optimal sample	4.15	0.20	4.6	28.36

4. Conclusions

$Nd_2Fe_{14}B$/2024Al composites with different Co contents were prepared by ball milling, cold isostatic pressing and microwave sintering. The results can be summarized as follows:

(1) When the sintering temperature was 490 °C, the heating rate was 20 °C/min, and the holding time was 30 min, with the Co content changing from 0→2.5%→5%→7.5%→10%, the grain size of the composites first decreased and then increased. The matrix grain size of the 7.5% Co sample was about 3–5 μm, and the compactness reached 95.4%, which were the optimal values.

(2) Through the nanoindentation test, the interface strength of the 7.5% Co sample was significantly higher than that of the sample without Co. In addition, its hardness, yield strength and compressive strength reached 152HV, 210 MPa and 269 Mpa, respectively, which increased by 67%, 78% and 75%, respectively, compared with the Co-free sample.

(3) With the increase in the Co content, the *B*r, and (*BH*) max of the composites first increased and then decreased, and when the Co content was 7.5%, all the three performance indicators reached their optimum, which were *B*r: 0.20 (T), H_{cj}: 4.6 (kOe) and (*BH*) max: 28.36 (kJ/m^3). The goal of lightweight of magnetic materials was preliminarily realized.

Author Contributions: Writing—original draft, T.Q.; Writing—review & editing, G.L. and H.W.; Resources, W.S.; Data curation, C.D.; Funding acquisition, J.Y. All authors have read and agreed to the published version of the manuscript.

Funding: This research was funded by the Postgraduate Research & Practice Innovation Program of Jiangsu Province (SJCX21_1704 and SJCX21_1705), "Intelligent Manufacturing Equipment Design and Engineering Application"-Excellent Science and Technology Innovation Team of Universities in Jiangsu Province (201907) and Jiangsu Intelligent Production Line Technology and Equipment Engineering Research Center (JDRC-HT-2019-1125).

Data Availability Statement: The datasets generated during and/or analyzed during the current study are available from the corresponding author on reasonable request.

Conflicts of Interest: The authors declare no conflict of interest.

References

1. Jiang, C.B.; An, S.Z. Recent progress in high temperature permanent magnetic materials. *Rare Met.* **2013**, *32*, 431–440. [CrossRef]
2. Tiwari, A. Magnetic Materials and Devices: Research and Applications. *JOM* **2011**, *63*, 24. [CrossRef]
3. Bai, G.; Gao, R.W.; Sun, Y.; Han, G.B.; Wang, B. Study of high-coercivity sintered NdFeB magnets. *J. Magn. Magn. Mater.* **2007**, *308*, 20–23. [CrossRef]
4. Chandan, B.; Kaustubh, A.; Sidananda, S. A new aluminum-based metal matrix composite reinforced with cobalt ferrite magnetic nanoparticle. *J. Mater. Sci.* **2013**, *48*, 162–171.
5. Fathy, A.; El-Kady, O.; Mohammed, M.M. Effect of iron addition on microstructure, mechanical and magnetic properties of Al-matrix composite produced by powder metallurgy route. *Trans. Nonferrous Met. Soc. China* **2015**, *25*, 46–53. [CrossRef]
6. Sadullahoglu, G.; Altuncevahir, B.; Addemir, O. Effect of Al and Cu Additions on Microstructure and Magnetic Properties of NdTb-FeCo-B Magnets. *Acta Phys. Pol. A* **2014**, *125*, 1172–1175. [CrossRef]
7. Batienkov, R.V.; Bol'shakova, A.N.; Khudnev, A.A. Microwave Sintering of Metal Powder Materials (Review). *Metallurgist* **2022**, *65*, 1163–1173. [CrossRef]
8. Wang, H.; Ren, W.; Li, G.; Wen, H.; Wang, C.; Chen, J.; Zhao, Y.; Chen, G.; Kai, X. Microstructure and properties of $FeCoNi_{1.5}CrCu$/2024Al composites prepared by microwave sintering. *Mater. Sci. Eng. A* **2021**, *801*, 140406. [CrossRef]
9. Kumar, M.A.; Seetharamu, S.; Nayak, J.; Satapathy, L.N. A Study on Thermal Behavior of Aluminum Cenosphere Powder Metallurgy Composites Sintered in Microwave. *Procedia Mater. Sci.* **2014**, *5*, 1066–1074. [CrossRef]
10. Li, G.R.; Xie, M.L.; Wang, H.M.; Xu, T.; Liu, M. Microstructure and properties of $Nd_2Fe_{14}B$ particles reinforced aluminum matrix composites synthesized by microwave sintering. *Mater. Res. Express* **2019**, *6*, 026538. [CrossRef]
11. Li, G.R.; Chen, J.J.; Zhang, D.; Wang, H.M.; Liu, M.; Tang, F.; Yan, Y.W.; Wen, H.R.; Ren, W.X.; Wang, C.W. Microstructure and properties of the $Nd_2Fe_{14}B_p$/Al-Co composites fabricated via microwave sintering. *J. Mater. Res. Technol.* **2021**, *10*, 34–50. [CrossRef]
12. Razzaq, A.M.; Majid, D.L.; Basheer, U.M.; Aljibori, H.S.S. Research Summary on the Processing, Mechanical and Tribological Properties of Aluminium Matrix Composites as Effected by Fly Ash Reinforcement. *Crystals* **2021**, *11*, 1212. [CrossRef]
13. Ao, M.; Liu, H.; Dong, C.; Feng, S.; Liu, J. Degradation mechanism of 6063 aluminium matrix composite reinforced with TiC and Al_2O_3 particles. *J. Alloys Compd.* **2021**, *859*, 157838. [CrossRef]
14. Khan, A.; Abdelrazeq, M.W.; Mattli, M.R.; Yusuf, M.M.; Alashraf, A.; Matli, P.R.; Shakoor, R.A. Structural and Mechanical Properties of Al-SiC-ZrO_2 Nanocomposites Fabricated by Microwave Sintering Technique. *Crystals* **2020**, *10*, 904. [CrossRef]
15. Mustofa, S.; Purwanto, S.; Sugeng, B.; Sudiro, T.; Hermanto, B.; Sudrajat, N. Early Characterization of NdFeB and NdFeB /Co-Al Composites of Sintering Using SPS. *Key Eng. Mater.* **2020**, *855*, 102–107. [CrossRef]
16. Melsheimer, A.; Seeger, M.; KronmuKller, H. Infuence of Co substitution in exchange coupled NdFeB nanocrystalline permanent magnets. *J. Magn. Magn. Mater.* **1999**, *202*, 458–464. [CrossRef]
17. Ghasali, E.; Pakseresht, A.; Safari-Kooshali, F.; Agheli, M.; Ebadzadeh, T. Investigation on microstructure and mechanical behavior of Al-ZrB_2 composite prepared by microwave and spark plasma sintering. *Mater. Sci. Eng. A* **2015**, *627*, 27–30. [CrossRef]
18. Sudharshan Phani, P.; Oliver, W.C.; Pharr, G.M. Measurement of hardness and elastic modulus by load and depth sensing indentation: Improvements to the technique based on continuous stiffness measurement. *J. Mater. Res.* **2021**, *36*, 2137–2153. [CrossRef]
19. Bushby, A.J. NANO-INDENTATION using spherical indenters. *Nondestruct. Test. Eval.* **2001**, *17*, 213–234. [CrossRef]

20. Ouyang, C.; Huang, M.; Li, Z.; Hu, L. Circular nano-indentation in particle-reinforced metal matrix composites: Simply uniformly distributed particles lead to complex nano-indentation response. *Comput. Mater. Sci.* **2010**, *47*, 940–950. [CrossRef]
21. Haghshenas, M.; Khalili, A.; Ranganathan, N. On room-temperature nanoindentation response of an Al-Li-Cu alloy. *Mater. Sci. Eng. A* **2016**, *676*, 20–27. [CrossRef]
22. Peng, H.; Tinga, W.R.; Sundararaj, U.; Eadie, R.L. Microwave sintering process model. *J. Microw. Power Electromagn. Energy* **2003**, *38*, 243–258. [CrossRef] [PubMed]
23. Willert-porada, M. Microwave sintering of hardmetals and ceramics. *Met. Powder Rep.* **1997**, *52*, 38.
24. Shestakov, V.A.; Korshunov, M.M.; Togushova, Y.N.; Dolgov, O.V. Decisive proofs of the transition in the temperature dependence of the magnetic penetration depth. *Supercond. Sci. Technol.* **2021**, *34*, 075008. [CrossRef]
25. Marc, A.M.; Chawla, K.K. Mechanical behavior of materials. *Aircr. Eng. Aero Technol.* **2008**, *81*, 83–85.
26. Boyle, K.P.; Curtin, W.A. Grain Interactions in Crystal Plasticity. *AIP Conf. Proc.* **2005**, *778*, 433–438.
27. Zhou, S.Z. *Ultra-Strong Permanent Magnet-Rare Earth Iron Permanent Magnet Materials*; Metallurgical Industry Press: Beijing, China, 1999; Volume 323.